



Cite as

Nano-Micro Lett.

(2024) 16:58

Received: 25 July 2023

Accepted: 8 November 2023

© The Author(s) 2023

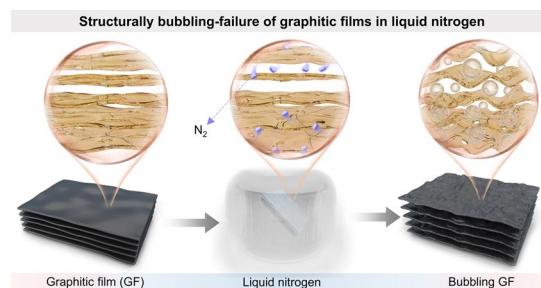
Highly Thermally Conductive and Structurally Ultra-Stable Graphitic Films with Seamless Heterointerfaces for Extreme Thermal Management

Peijuan Zhang¹, Yuanyuan Hao¹, Hang Shi¹, Jiahao Lu¹, Yingjun Liu^{1,2} ✉, Xin Ming¹ ✉, Ya Wang^{1,7}, Wenzhang Fang¹, Yuxing Xia¹, Yance Chen¹, Peng Li¹, Ziqiu Wang¹, Qingyun Su³, Weidong Lv⁴, Ji Zhou⁴, Ying Zhang⁵, Haiwen Lai⁶, Weiwei Gao^{1,2}, Zhen Xu^{1,2} ✉, Chao Gao^{1,2} ✉

HIGHLIGHTS

- Presenting the first investigation into the structurally bubbling-failure mechanism of graphitic film during cyclic liquid nitrogen shocks.
- Proposing an innovative design about seamless heterointerface constructing a Cu-modified structure.
- Inventing a new ultra-stable species of highly thermally conductive films to inspire new techniques for efficient and extreme thermal management.

ABSTRACT Highly thermally conductive graphitic film (GF) materials have become a competitive solution for the thermal management of high-power electronic devices. However, their catastrophic structural failure under extreme alternating thermal/cold shock poses a significant challenge to reliability and safety. Here, we present the first investigation into the structural failure mechanism of GF during cyclic liquid nitrogen shocks (LNS), which reveals a bubbling process characterized by “permeation-diffusion-deformation” phenomenon. To overcome this long-standing structural weakness, a novel metal-nanoarmor strategy is proposed to construct a Cu-modified graphitic film (GF@Cu) with seamless heterointerface. This well-designed interface ensures superior structural stability for GF@Cu after hundreds of LNS cycles from 77 to 300 K. Moreover, GF@Cu maintains high thermal conductivity up to $1088 \text{ W m}^{-1} \text{ K}^{-1}$ with degradation of less than 5% even after 150 LNS cycles, superior to that of pure GF (50% degradation). Our work not only offers an opportunity to improve the robustness of graphitic films by the rational structural design but also facilitates the applications of thermally conductive carbon-based materials for future extreme thermal management in complex aerospace electronics.



KEYWORDS Highly thermally conductive; Structurally ultra-stable; Graphitic film; Extreme thermal management; Liquid nitrogen bubbling

✉ Yingjun Liu, yingjunliu@zju.edu.cn; Xin Ming, xin_ming@zju.edu.cn; Zhen Xu, zhenxu@zju.edu.cn; Chao Gao, chaogao@zju.edu.cn

¹ MOE Key Laboratory of Macromolecular Synthesis and Functionalization, Department of Polymer Science and Engineering, Key Laboratory of Adsorption and Separation Materials and Technologies of Zhejiang Province, Zhejiang University, 38 Zheda Road, Hangzhou 310027, People's Republic of China

² Shanxi-Zheda Institute of Advanced Materials and Chemical Engineering, Taiyuan 030032, People's Republic of China

³ Beijing Spacecrafts Manufacturing Co., Ltd, Beijing Friendship Road 104, Haidian District, Beijing 100094, People's Republic of China

⁴ Beijing Institute of Space Mechanics and Electricity, Beijing Friendship Road 104, Haidian District, Beijing 100094, People's Republic of China

⁵ China Academy of Aerospace Aerodynamics, Beijing 100074, People's Republic of China

⁶ Hangzhou Gaoxi Technol Co., Ltd, Hangzhou 311113, People's Republic of China

⁷ International Research Center for X Polymers, International Campus, Zhejiang University, Haining 314400, People's Republic of China

Published online: 19 December 2023



SHANGHAI JIAO TONG UNIVERSITY PRESS

Springer

1 Introduction

The continuing miniaturization and integration of ultra-fast high-frequency electronic devices have led to significant challenges in efficient thermal management, as it inevitably increases temperature and reduces reliability [1–3]. These challenges are particularly apparent in complex operating conditions, such as militaries [4], spacecrafts [5], supercomputers [6], nuclear reactors [7–9], and other complex scenarios. Some common environmental factors in these extreme application scenarios like temperature variations [10, 11], ultraviolet irradiation [12], atomic oxygen [12], and liquid nitrogen [13–15] can significantly impact the stability of devices, setting new requirements for thermal management materials.

Liquid nitrogen, with its incredibly low temperature of 77 K, is a versatile cold source used in nuclear power plants and aerospace [15–17]. Heat dissipation includes the process of heat production from devices, heat transfer (heat conduction) by thermal management materials, and cooling by cold source. In these special working scenarios, mass waste heat generated by high-power devices (heat source) could be conducted into liquid nitrogen (cold source) through a heat transfer medium [16, 17]. However, this technology faces challenges due to the exceptionally low temperature, high surface tension, and significant volume expansion under temperature changes of liquid nitrogen [18]. These factors can lead to unavoidable structural damage of functional parts under such complicated service conditions, thereby degrading heat dissipation performance. Therefore, achieving the integration of structural stability and high-performance material design under extreme conditions is a critical challenge in the field of thermal management.

Thermal management materials including polymers [19–21], ceramics [22–29], and metals [30–32] have been extensively utilized and developed. Due to their inherent drawbacks, they are unable to meet the demand for complex and extreme scenarios. Carbon-based materials [33–44], such as highly thermally conductive graphitic film (GF) with the combined merits of low density, outstanding flexibility, low thermal expansion coefficient, and intrinsic chemical resistance offer a promising alternative to traditional thermal conductive materials [45–48]. At present, there are two main ways to achieve high structure stability and performance at room temperature, including the interlayer crosslinking

strategy [49, 50] and the plasticizing orientation method [51, 52]. However, utilizing cross-linked polymers would reduce the thermal conductivity, and plasticization stretching could only eliminate the partial internal defects of films, but its intrinsic structural instability could not be solved under extreme conditions. Besides, these methods are mainly concerned with film properties at room temperature. There are few studies on the structural stability and durability of GF in extreme scenarios (Fig. 1a), such as liquid nitrogen cyclic thermal management in nuclear power plants [15] and compute overclocking operation [16, 53]; extremely low or high temperatures from -180 to $+180$ °C in space; low-temperature service scene of electric vehicle in the cold regions. We wonder if GF can endure the cyclic liquid nitrogen shock (LNS) without sacrificing its thermal properties to achieve long-term stability.

Here, we report the unusual bubbling phenomenon of GF during LNS for the first time and uncover the structural failure mechanism. The bubbling process is related to the permeation and diffusion of N_2 molecules in the crevices and inner voids of GF. To overcome this issue, we further propose a novel metal-nanoarmor strategy involving sputtering copper coatings on both surfaces of GF (GF@Cu). This well-designed seamless heterogeneous structure provides superior structural stability of GF@Cu after hundreds of LNS from 77 to 300 K. The GF@Cu exhibits a high thermal conductivity up to $1088 \text{ W m}^{-1} \text{ K}^{-1}$, with a retention ratio higher than 95%, which greatly exceeds that of pure GF ($\sim 50\%$ degradation). Furthermore, the seamless interface design also ensures improved mechanics, electricity, and magnetism properties compared to the original GF. This study overcomes the intrinsic structural instability of highly thermally conductive GF in extreme liquid nitrogen oscillation environments. Additionally, the revealed failure mechanism of cyclic LNS and the metal-nanoarmor strategy with seamless interface provide inspiration for the development of extreme thermal management materials and technologies.

2 Experimental Section

2.1 Materials

Highly thermally conductive graphitic films were purchased from Hangzhou Gaoxi Technology Co., Ltd (www.gaoxi.com)

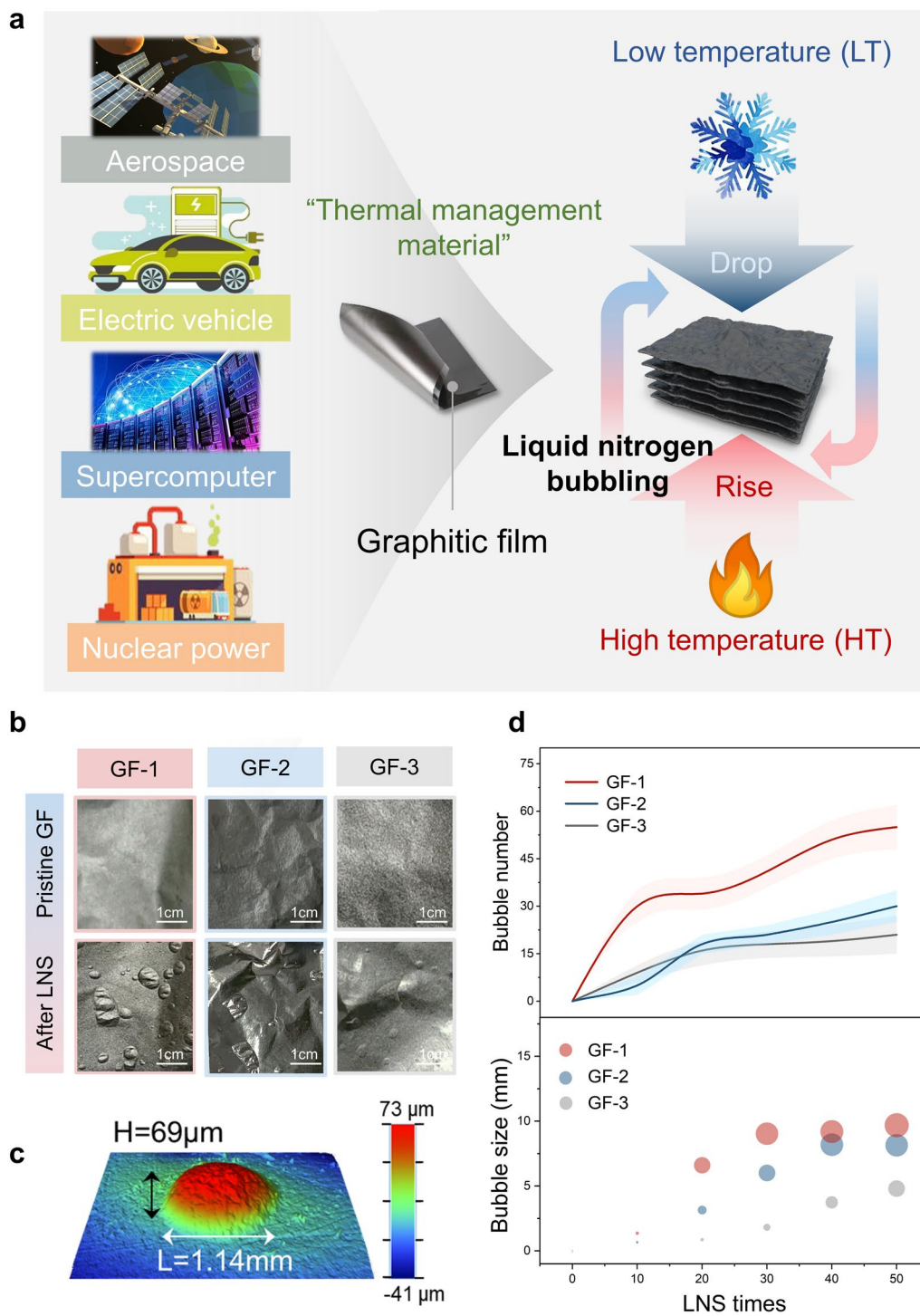


Fig. 1 Structurally bubbling-failure mechanism of GF during extreme environment. **a** Schematic illustration of GF applied in temperature fluctuation scenarios. **b** Morphologies of different GFs before and after LNS. **c** Stereoscopic structure image of a typical bubble. **d** The number and size of bubbles on the surface of GFs vary with the number of LNS

tech.com). All chemicals were analytically pure, all materials were used as received.

2.2 Preparation of Cu-modified Graphitic Film (GF@Cu)

Cu coating (~240 nm) has been deposited by magnetron sputtering at an Ar partial pressure of 4.5×10^{-2} mbar, with a vacuum of 10^{-5} mbar, with a cathode power of 120 W onto graphitic film substrates for 30 min. The graphitic films were already cleaned with ethanol.

2.3 Characterizations

The instrument used for magnetron sputtering was Kurt J. Lesker PVD 75. Stereoscopic structure images were taken by the white-light interferometer (Wyko NT9100). The microstructure and mapping of GF@Cu were characterized by a field-emission scanning electron microscope (SEM) with energy dispersive X-ray (Hitachi S4800). Internal structure images were obtained by a focused ion beam and imaged on the same instrument (Carl Zeiss Auriga 40). X-ray diffraction (XRD) was performed with an X'Pert Pro (PANalytical) diffractometer using monochromatic Cu K α 1 radiation ($\lambda = 1.5406 \text{ \AA}$) at 40 kV. X-ray photoelectron spectroscopy (XPS) characterization was conducted using a ThermoFisher Escalab 250Xi instrument and all binding energies were referenced to the C 1s neutral carbon peak at 284.8 eV. Raman spectroscopy and mapping scanning were recorded by a commercial Renishaw in a Via-Reflex Raman microscope at an excitation wavelength of 532 nm. Nanoindentation experiments were conducted at a constant temperature of 20 °C on Agilent Nano Indenter G200 with a standard Berkovich indenter. The thermal conductivity was evaluated by NETZSCH LFA467 HyperFlash at room temperature, which could obtain a relatively effective value of in-plane thermal conductivity of the thin film with a similar layered structure. The interfacial microstructure of GF@Cu was observed by scanning transmission electron microscope (Titan ChemiSTEM). Transmission electron microscope samples were prepared by a focused ion beam (FIB) machine (Nova 600, FEI). Tensile strength tests were conducted using an Instron 2344 at a loading rate of 5 mm min^{-1} , and the size of the tested strip is 20 mm (length) \times 1 mm (width). The gauge length is 10 mm. The bend speed was about six cycles per

minute in the bending test. The electrical conductivity and resistance were measured using a standard four-probe method on a Keithley 2460 multiple-function source meter. An infrared camera (FLIR T630sc) was used to measure the temperature profile along with the film strips. The EMI SE performance was tested by a vector network analyzer (ZNB-40, Rohde & Schwarz, Germany).

3 Results and Discussion

3.1 Environmental Tolerance and Bubbling Failure of GF

To investigate the tolerance of GF in extreme environments, specifically rapid shocks from air to liquid nitrogen, a cyclic LNS test is introduced. The GFs were repeatedly subjected to LNS to assess their structural robustness (Fig. 1a). All three GFs exhibit an obvious bubbling phenomenon and the number of bubbles increases with LNS times, indicating serious structural damage (Figs. 1b and S1). Similarly, this bubbling phenomenon is also observed in the graphene film (Fig. S2), indicating that it may be a common phenomenon in carbon-based films. A typical morphology of a bubble with a length of 1.14 mm and a height of 69 μm is illustrated in Fig. 1c (additional optical profiler images of bubbles are provided in Fig. S3). The bubble evolution processes in all GFs are evaluated with LNS times, showing a significant positive correlation between the LNS times and the number/size of bubbles on the surface of GF (Fig. 1d). This bubbling process follows the classical nucleation-growth model [54, 55]. Furthermore, it is observed that GF with higher density tends to exhibit fewer numbers and smaller size bubbles per unit area (Fig. S4), indicating a relationship between the compactness structure of GF and the bubbling degree. Among them, when GF-1 with a density of 1.84 g cm^{-3} suffered from 50 times LNS, the number of bubbles reached an astonishing 55, and its bubble size was up to 9.68 mm.

3.2 Structural Failure Mechanism and Molecular Dynamics Simulation of Bubbling Process in GF

To uncover the possible mechanism of bubbling process during LNS, the GF immersed directly in liquid nitrogen was compared with the GF experienced LNS without contact

with liquid nitrogen by plastic sealing. The latter shows no bubbles on the surface (Fig. S5). Hence, these results suggest that the interaction between liquid nitrogen molecules and GF is a key factor in the bubble formation process. A structural failure mechanism is proposed to elucidate the bubbling process of GF during LNS, as depicted in Fig. 2a. When GF is immersed in liquid nitrogen, N_2 molecules permeate through the surface crevices (Fig. 2b) and accumulate within the inner voids of the GF due to the ultralow critical diffusion resistance [56, 57]. Upon moving the GF into the air, the sudden temperature change triggers the transition of the N_2 permeated in the GF from the liquid phase to the gas phase, leading to huge volume expansion (~ 648 times expansion in unconfined space) and local layer deformation. This deformation ultimately results in the formation of bubbles, which is also consistent with our observations in the practical LNS tests (see Video S1), where the surface bubbles fast expand as the liquid nitrogen evaporates. To further support our proposed mechanism, the cross-sections of GF were observed through the FIB-SEM system (Fig. 2c). There are voids between the layers of GF, which are related to the assembly of precursor in fabrication process and the escape of volatile components during post-processing stage [58–60]. Furthermore, comparable internal structures are also observed in several GFs that exhibit bubbling during LNS (Fig. S6). The consistent thickness observed in the bubble walls ($\sim 9 \mu\text{m}$) and the void depth ($\sim 9 \mu\text{m}$) also provides evidence for this structural failure mechanism (Fig. 2c).

To further verify the mechanism that the crevices and inner voids in GF facilitate the diffusion of N_2 and subsequent bubble formation, we conducted molecular dynamics simulations to explore the interaction between N_2 and graphene sheets under alternating temperature conditions (further details can be found in the Supporting Information). It is evident that N_2 molecules exhibit continued diffusion at a temperature of 77 K with low drag, resulting in a gradual accumulation of N_2 molecules in the interlayer spaces of graphene (Fig. 2d, h). N_2 molecules diffusion process can also be illustrated from the mean square displacements (MSD) curve (Fig. 2f), whose slope contains information about the degree of diffusion. The diffusion coefficient ($1.48 \times 10^{-8} \text{ m}^2 \text{ s}^{-1}$) for N_2 molecules is calculated from their mean square displacements, indicating that N_2 molecules can diffuse into the graphene sheets. Upon increasing the temperature to 300 K, the graphene sheets show significant deformation of $\sim 0.12 \text{ \AA}$ in the perpendicular direction to

the surface, which is consistent with the observed bubbling process (Figs. 2e, g and S7). Therefore, the structural failure behavior of the GF is strongly related to the surface and internal defects, which provides theoretical guidance for improving the structural stability of GF during cyclic LNS.

3.3 Construction and Characterization of Seamless Heterointerface

To enhance the structural stability of GF and ensure their high performance in extreme environments, it is crucial to mitigate the defect constraint on the surface. A novel metal-nanoarmor strategy is proposed to construct a seamless heterogeneous interface on the surface of GF by using magnetron sputtering ultra-thin Cu layer (Fig. 3a), which could suppress bubbles by restrain the bubble nucleation and growth from Henry theory [54]. The GF@Cu possesses a compact and uniform Cu layer with $\sim 240 \text{ nm}$ (Figs. 3b and S8, S9), showing characteristic peak of Cu element in XPS spectra (Fig. S10). From the density functional theory (DFT) calculation, the interfacial strength at Cu/graphene interface of 0.516 J m^{-2} is significantly higher than that of the graphene/graphene interface (0.259 J m^{-2}), which is attributed to the strong interaction of Cu $3d$ and C $2p$ states. The charge transfer between interfacial atoms leads to strong interfacial strength (Fig. S11). Moreover, the GF@Cu with seamless interface retains the same graphitization degree as the original GF, indicating that the crystal structure of graphite layer is not significantly damaged (Fig. S12). The ultra-thin and seamless heterogeneous interface structure of GF@Cu could effectively prevent the diffusion of N_2 molecules via defect on the surface (Fig. 3c), resulted from the defect density decreased from $\sim 9.6\%$ to $\sim 0\%$ compared to the original GF (Figs. S13 and S15). This enhanced seamless heterointerface can effectively restrain the diffusion of N_2 molecules and then reduce the bubble nucleation (Fig. S13). The molecular dynamics results also show that the addition of nano-metal armor effectively reduces the accumulation of N_2 in the interior and thus could decrease the probability of nucleation to avoid catastrophic bubbling (Fig. 3g, h). Meanwhile, the seamless heterointerface could effectively inhibit bubble growth through enhanced surface mechanical properties. Nano-indentation micromechanical characterization was

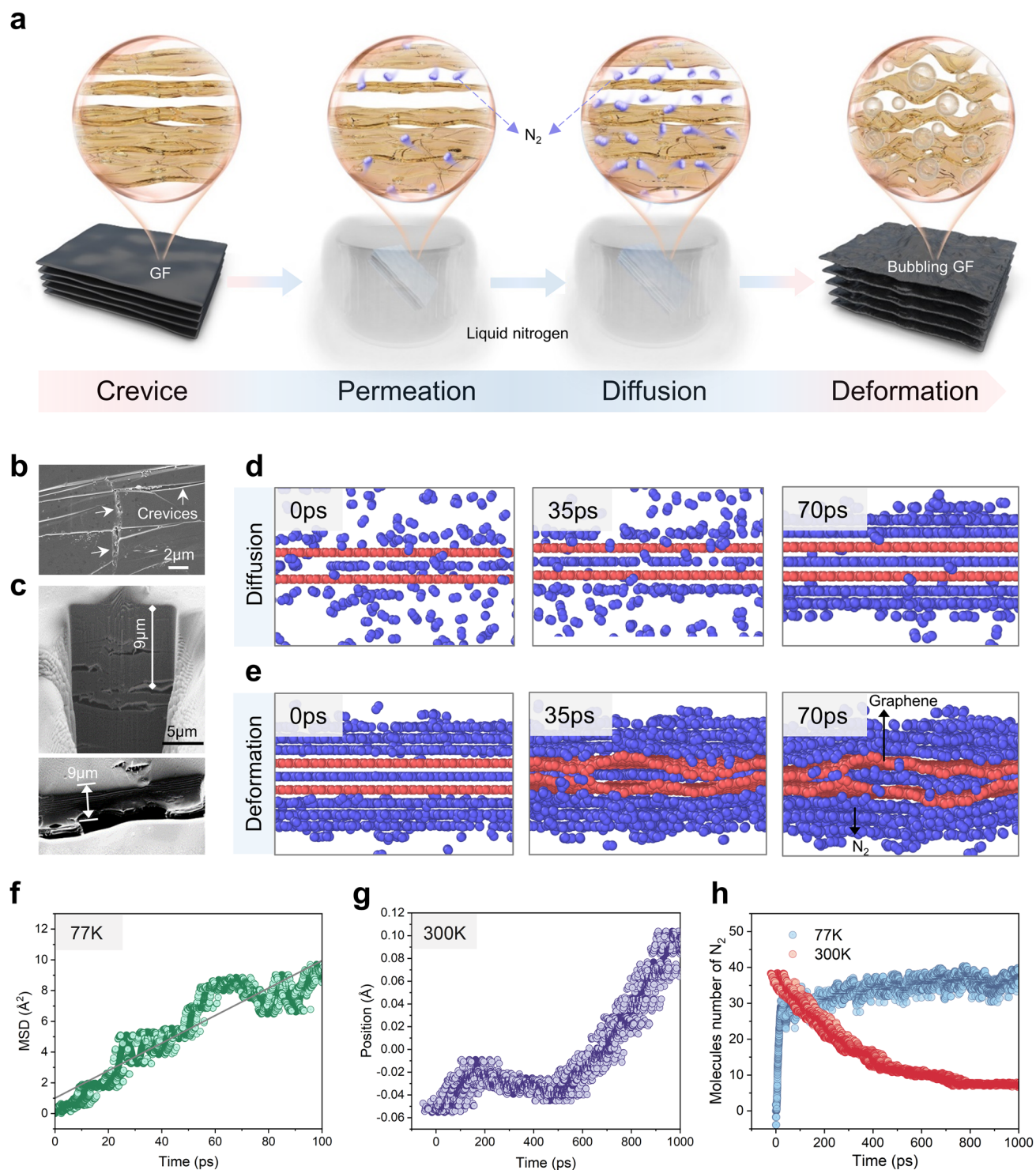


Fig. 2 Structural failure mechanism of GF during cyclic LNS. **a** Schematic diagram of GF deformation caused by N₂ molecules. **b** SEM image of the crevices on GF. **c** SEM images of the internal structure of GF and the bubble wall, obtained by using a focused ion beam cutting. **d** Corresponding 3D rendering of N₂ molecules diffuse over time at liquid nitrogen temperature (77 K). **e** Corresponding 3D rendering of N₂ molecules diffuse over time as the ambient temperature becomes room temperature (300 K). **f** The mean square displacements (MSD) of N₂ molecules from MD simulations at 77 K. **g** The average position of the graphene sheet in a nitrogen environment from MD simulations at 300 K. The position in center of two graphene sheets slit is defined as 0. **h** Molecules number of N₂ between graphene sheets over time from MD simulations at different temperatures

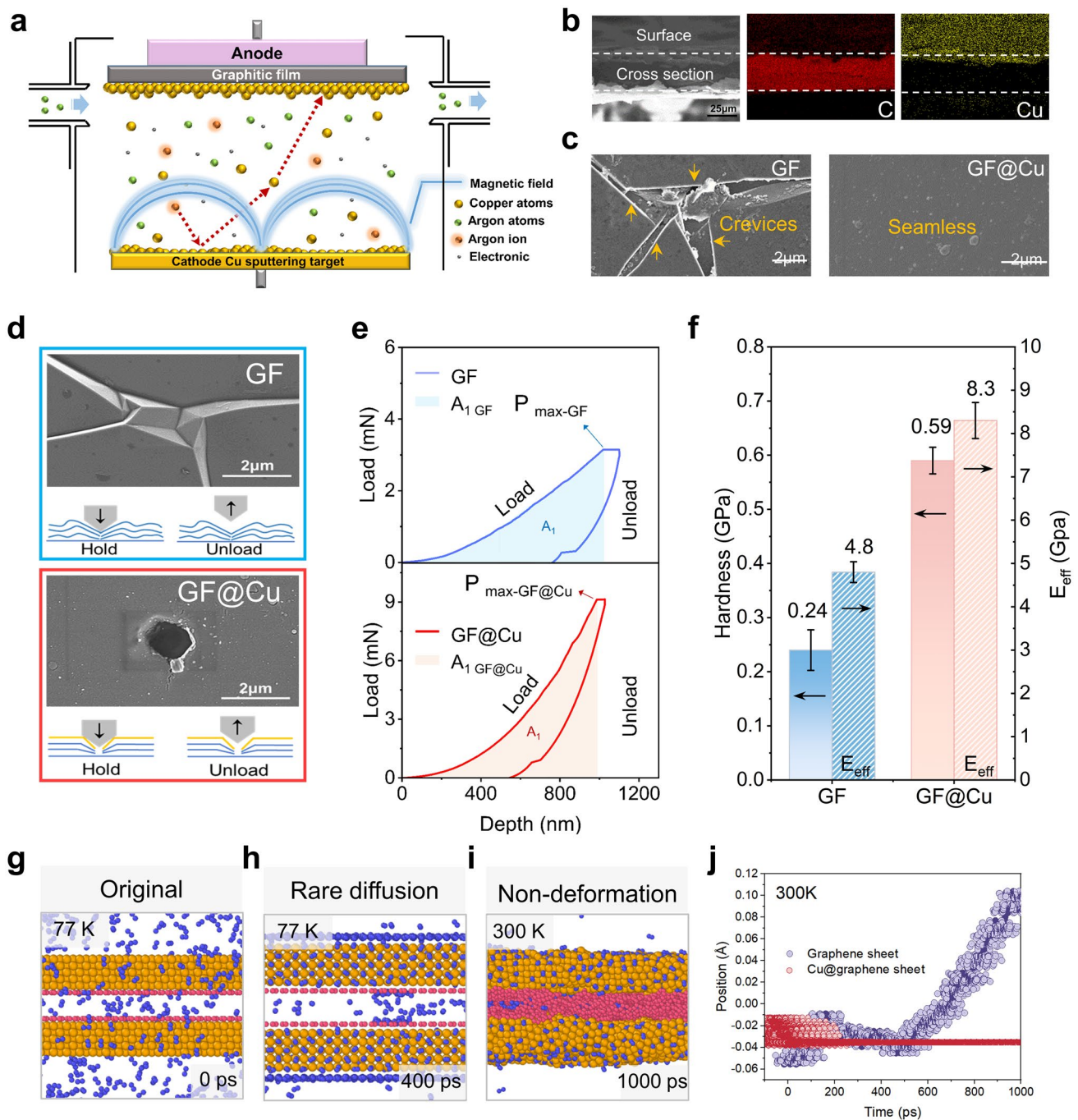


Fig. 3 Design of seamless heterointerface constructing a Cu-modified structure. **a** Schematic diagram of magnetron sputtering coating with Cu on the surface of GF. **b** Cross-sectional energy dispersive X-ray (EDX) mapping of GF@Cu. **c** SEM images of the surface of GF and GF@Cu. **d** Morphology inspection of indentation on GF and GF@Cu surface after nanoindentation test. **e** Force versus depth curves of GF and GF@Cu by nanoindentation. **f** Hardness and effective Young's modulus of GF and GF@Cu. **g** Corresponding 3D rendering of Cu@graphene sheet under liquid nitrogen environment (77 K). **h** Corresponding 3D rendering of rare N₂ molecules diffuse into Cu@graphene slit over time at liquid nitrogen temperature (77 K). **i** Corresponding 3D rendering of Cu@graphene sheets hardly deform as the ambient temperature becomes room temperature (300 K). **j** The average position of the graphene sheet and Cu@graphene sheet in a nitrogen environment from MD simulations at 300 K. The position in center of two graphene sheets slit is defined as 0

employed to explore the surface deformability of both the GF and the GF@Cu to elucidate the enhancement mechanism for seamless heterogeneous interface. A permanent inverted hole is generated on the surface of the GF and the GF@Cu by the Berkovich indenter (Figs. 3d and S16). It is evident that the GF without seamless interface has undergone greater deformation as measured by the area of the hole (Table S1). Additionally, the load-depth curve shows that more energy is required to conquer the same depth in the GF@Cu with seamless interface ($A_{1\text{ GF@Cu}} > A_{1\text{ GF}}$) (Fig. 3e).

The hardness value of GF@Cu is determined to be 0.59 GPa, which guarantees less deformation, while the hardness of GF is only 0.24 GPa (Fig. 3f). Similarly, the effective Young's modulus (E_{eff}) of both films also reflect that the seamless interface could enhance the resistance to deformation under a given stress. The $E_{\text{eff GF@Cu}}$ (8.3 GPa) is significantly higher than $E_{\text{eff GF}}$ (4.8 GPa) (Fig. 3f). The superior hardness and E_{eff} of GF@Cu with seamless interface confirm its advantages in enhancing deformation resistance, which is essential for reducing complex mechanical damage caused by extreme liquid nitrogen expansion during LNS. This mechanical enhancement would lead to a significant increment in the surrounding pressure of bubble which should be overcome in bubble growth (Fig. S14), and further inhibit the growth of bubbles (Fig. S13). The effectiveness of our seamless heterointerface is also verified by molecular dynamics simulations. The lamellar deformation caused by liquid nitrogen gasification of the model with copper atomic layer is significantly smaller than that of pure graphene film (Fig. 3i, j). Additionally, the penetration of N_2 during LNS is significantly hindered by the protection of metal-nano armor, which would weaken the ability of the bubble growth endowed by the concentration of N_2 (Figs. S13, S14). The metal-nano armor strategy guidance with seamless interface shows great promise for enhancing the structural stability of conventional GF in extreme environments to conduct thermal management.

3.4 Effects of Seamless Heterointerface on the Thermal Conductivity of GF

The seamless heterointerface has been proven to play an important role in maintaining the structural stability of GF

for achieving stable performance. We comprehensively investigated the effect of the seamless heterogeneous interface on the thermal transport of the GF after LNS. When exposed to an equivalent 150 times LNS, the GF@Cu presents a distinctly smooth surface compared with the bubbling surface of GF (Figs. 1b and 4a, b), attributed to the impervious seamless heterointerface. Besides, the interface connection of Cu@GF between the seamless heterointerfaces and the GF substrate is still tight after cyclic LNS (Fig. S17). As a consequence, the interior structure of GF@Cu remains non-penetration, thereby avoiding extensive structural destruction by LNS. As shown in Fig. 4c, the thermal conductivity of the GF drastically decreases by almost 50% from 1312 to 728 $\text{W m}^{-1} \text{K}^{-1}$ after 150 times LNS. In contrast, the GF@Cu displays higher thermal conductivity retention up to 96%, changing from 1137 to 1088 $\text{W m}^{-1} \text{K}^{-1}$ after the same time LNS. The corresponding infrared image of the GF@Cu with seamless heterointerface also demonstrates stable thermal transfer performance after LNS, while the structural failure of GF seriously disturbs its heat transfer (Figs. 4d, e and S18). Furthermore, it is worth mentioning that the thermal conductivity of the GF@Cu is slightly lower than that of the theoretical value, according to the classical composite parallel model (Fig. S19). The finite element simulation suggests the interface plays a non-negligible role in this weak reduction of thermal conductivity of GF@Cu with seamless interface before LNS (Fig. S20). When the GF is sputtered with seamless heterogeneous interface, the phonon coupling between Cu and C dominates the interfacial heat transport, and the electron coupling between Cu and C provides an additional heat transport pathway along the C/Cu interface [59]. However, the high-energy magnetron-sputtering-deposited method would generate the inevitable interfacial defects of substrate materials, and the additional defects would impede the interfacial heat transport, thus leading to decreased thermal conductivity [60–63] (Fig. 4f).

To explore this interfacial structure evolution and reveal the atomic origins of the reduction of thermal conductivity, we observed the heterointerface by atomically resolved Aberration Corrected Scanning Transmission Electron Microscopy (AC-STEM). As shown in Fig. 4g, there is an obvious penetration of C and Cu elements at the interface while in the corresponding bulk parts they are homogeneously distributed. According to the AC-STEM (Fig. 4h), the bulk of GF has a typical layered graphene morphology with a layer spacing of 0.34 nm, indicating a high crystallinity

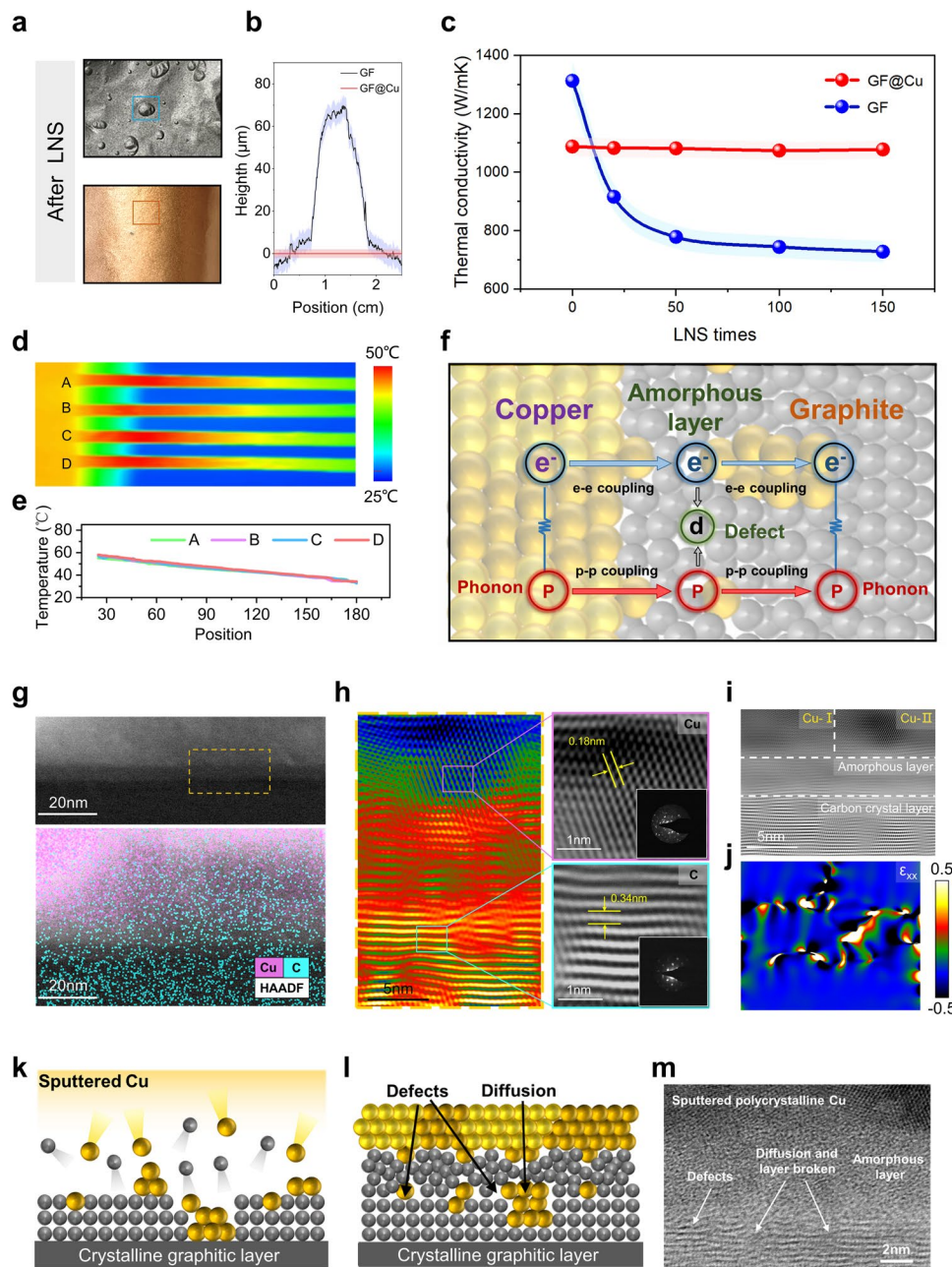


Fig. 4 Effects of seamless heterointerface on the thermal conductivity of GF. **a** Digital images and **b** surface information of GF and GF@Cu after 150 times LNS. **c** Thermal conductivity of GF and GF@Cu varies with the number of LNS times. **d** Infrared image of GF@Cu and **e** temperature profiles with different LNS times, A=0 times, B=50 times, C=100 times, D=150 times. **f** Schematic diagram about heat transport mechanisms at Cu/C interface. The possible heat transport pathways at interface include: the phonon coupling between C and Cu, the electron coupling between C and Cu and interface defect. **g** Element distribution of the Cu/C structure, the HAADF mapping shows interfacial mixing layer forms at the C/Cu interface. **h-i** AC-STEM images of the Cu/C interface. **j** Analysis on local strain of Cu/C interface. **k-l** Cross-sectional schematics and **m** TEM image of magnetron-sputtering-deposited Cu on the surface of GF, where the bombardment of the GF surface by high-energy Cu atoms and clusters creates considerable damage to the GF surface, producing an amorphous layer with apparent defects, interface diffusion, atomic disorder and interfacial stress

to ensure ultra-high thermal conductivity. Meanwhile, the bulk Cu layer at the interface shows a polycrystalline structure, ensuring the sealing function of seamless heterogeneous interface. It is clear that an amorphous layer (a-L) of ~ 5 nm exists at the C/Cu interface, caused by high-energy atom bombardment during magnetron sputtering (Fig. 4i). Therefore, the total thermal resistance (R_{total}) of the C/Cu interface actually could be considered as the sum of the thermal resistance of a-L ($R_{\text{a-L}}$) and the interface itself ($R_{\text{C/a-L}} + R_{\text{a-L/Cu}}$). The increase of defect density within the a-L could lead to the increment of the corresponding $R_{\text{a-L}}$ [64]. Simultaneously, the mismatch of electron density and vibrational density of states at the GF/Cu interface also leads the transport of electrons and phonons to be blocked, resulting in high interfacial thermal resistance at nanoscale [65]. Furthermore, the drastic interface local strain accompanied by high density of defects in the C/Cu interface is inferred to reduce phonon scattering relaxation time and increase phonon thermal resistance [64] (Fig. 4j). The bombardment of high-energy Cu atoms during magnetron sputtering preparation is responsible for inevitably generating apparent defects, interface diffusion, atomic disorder and interfacial stress [66], which are obviously characterized in the TEM image of C/Cu interface (Fig. 4k–m). The appearance of Raman D peak on the surface of the GF@Cu after removing Cu layers also confirms the introduction of defects in the magnetron sputtering process (Fig. S21). Therefore, the existence of R_{total} in the nanoscale C/Cu interface would slightly reduce the thermal conductivity of GF@Cu. It is worth mentioning that this ultra-thin seamless heterointerface can greatly improve the structural stability to maintain the high thermal conductivity of GF after numerous LNS times, so as to meet the needs of extreme thermal management in the future.

3.5 Comprehensive Functional Performance of GF@Cu for Practical Applications

The comprehensive performances of GF@Cu with seamless heterointerface are investigated to verify its potential in practical applications. The electrical conductivity of the GF@Cu remains $1.1 \times 10^6 \text{ S m}^{-1}$, which is higher than that ($0.9 \times 10^6 \text{ S m}^{-1}$) of the GF after 150 times LNS (Fig. S22). The increment of electrical conductivity is attributed to the combination of high carrier density of Cu and high mobility of GF [67]. Therefore, the GF@Cu with seamless heterointerface

can also be used as a potential electromagnetic interference (EMI) shielding material [68–70]. Compared with the original GF, the EMI shielding effectiveness (EMI SE) of the GF@Cu is significantly improved, which increases from 65.4–70.3 to 74.1–79.0 dB in 8–12 GHz (Fig. S23), due to the enhanced electromagnetic field reflection loss from the highly conductive copper coating and electromagnetic field absorption loss from thicker film (Fig. S24). In terms of mechanical properties, the structure of the GF has been damaged after LNS, and its tensile strength and elongation at breakage both decrease sharply (Fig. 5a). However, the tensile strength and elongation of GF@Cu are well maintained, contributed by the repair of surface defects and the effective composite with the reinforcement phase (Cu). The tensile strength of GF@Cu is 49 MPa, ~ 9 times higher than that (5 MPa) of GF after LNS. Besides, the resistance and the coating bond of GF@Cu barely changes after 1000 bending-releasing cycles, suggesting a high tolerance for bending deformation (Figs. 5d and S17, S25). The GF@Cu demonstrates remarkable flexibility, possessing the ability to maintain structural integrity even after undergoing harsh deformation, such as repetitive bending (Fig. 5d), twisting, and complex folding of a paper crane, without incurring any breaks or fractures (Fig. 5e). Furthermore, aided by inherent flexibility of GF@Cu, the stretchable cooling components can be designed through kirigami to meet future special-shaped heat dissipation requirements (Fig. 5b). Meanwhile, the highly thermally conductive and ultra-stable GF@Cu can achieve effective heat dissipation of liquid nitrogen as an extreme cold source, inspiring new technologies for thermal management. It effectively makes temperature of heat source drop by 21 °C in two minutes (Fig. 5c). By introducing a seamless heterointerface, the GF@Cu shows a substantial improvement in thermal, mechanical, electrical performances, and stability (Fig. 5f and Table S2). Furthermore, we use different films as heat diffusion materials for a high-power LED lamp, which could verify the performance stability of modified Cu@GF than pristine GF for effective operation in extremely cold sources (Figs. 5g, h and S26). As displayed in Fig. 5g–i, the LED lamp equipped with the GF@Cu as a thermal spreader exhibits a similar heat-spot temperature with pure GF after 180 s of work, and the LED lamp equipped with the GF@Cu after LNS as a thermal spreader exhibits lower heat-spot temperature of about 0.8 °C than pure GF after LNS after 180 s. These results indicate the GF@Cu not only possesses a higher thermal conductivity but also

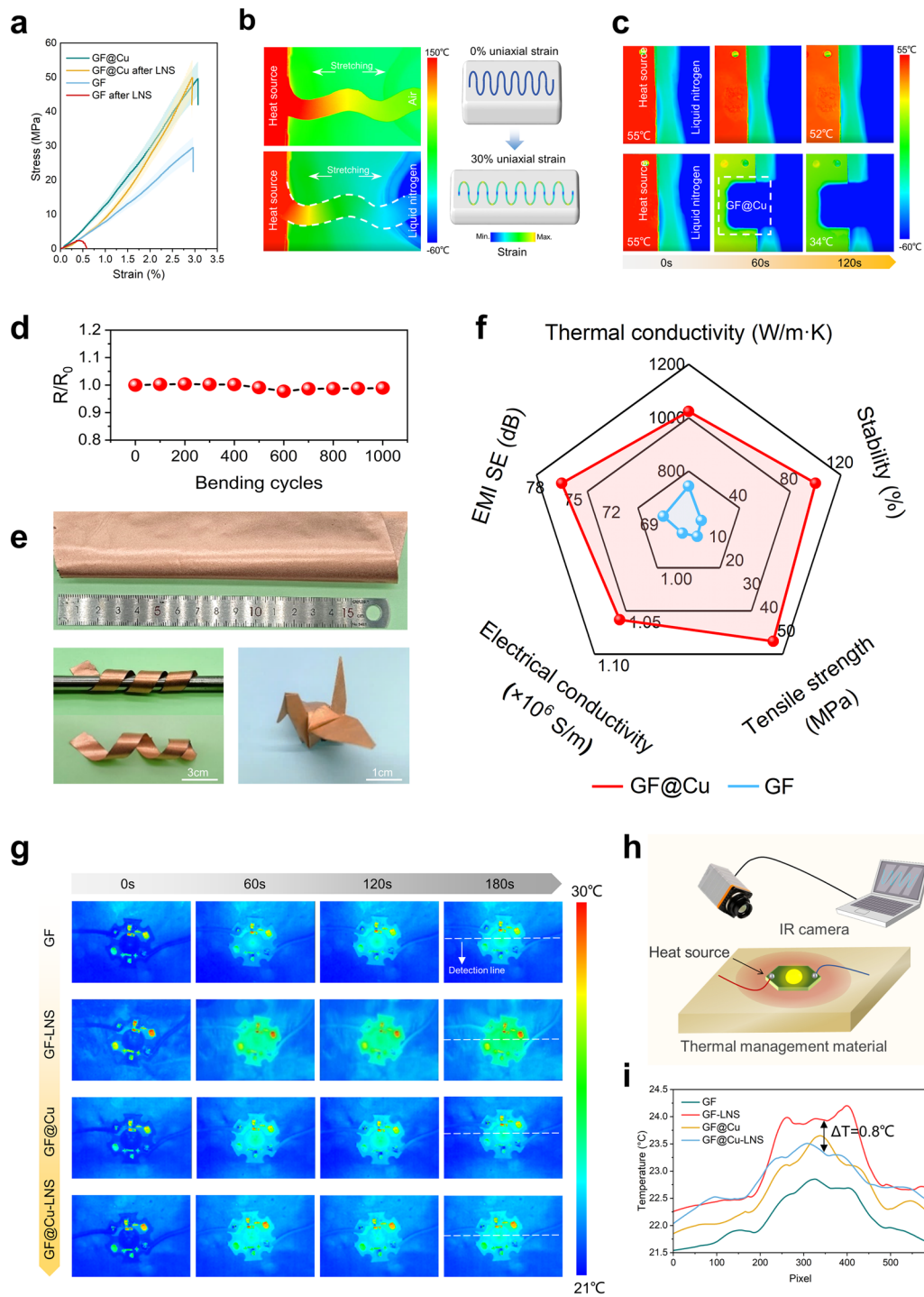


Fig. 5 Comprehensive functional performance of GF@Cu for practical applications. **a** Tensile stress–strain curves of GF and GF@Cu. **b** Infrared images and schematic diagrams of GF@Cu as a stretchable and stable thermal management module in extreme environment from 77 to 300 K. **c** Infrared images of heat dissipation application conducted by GF@Cu with liquid nitrogen as cold source. **d** Relative resistance variation of GF@Cu under cyclic bending 1000 times. **e** GF@Cu with the state of bending, twisting, and folding into a crane without breakages. **f** Overall performances of GF@Cu (red line) and GF (blue line). Stability is defined as 100% when no structural damage occurs for ≥ 100 LNS, and stability is defined as the number of shocks when bubbles occur for < 100 LNS. **g** Infrared images of an LED lamp with different films for heat dissipation. **h** Schematic diagram of films as heat diffusion materials for a high-power LED lamp. **i** Temperature profiles which are plotted by infrared images

relieves the possible urgent thermal management demands in a hostile environment.

4 Conclusion

In summary, we report the undetected structural instability phenomenon of GF in response to cyclic LNS and reveal the structural failure mechanism, which follows the “permeation-diffusion-deformation” bubbling process of N_2 molecules in the crevices and inner voids of GF. To avoid this failure, we propose a novel metal-nano armor strategy involving constructing a copper-modified graphitic film (GF@Cu) with seamless heterointerface. This well-designed interface provides superior structural stability of GF@Cu after even hundreds of LNS from 77 to 300 K. The GF@Cu maintains high thermal conductivity up to $1088 \text{ W m}^{-1} \text{ K}^{-1}$, with a degradation of less than 5%, significantly superior to that of pure GF (~50% degradation). Additionally, the GF@Cu exhibits excellent electrical conductivity ($\approx 1.1 \times 10^6 \text{ S m}^{-1}$), enhanced EMI SE performance and more stable mechanical performance, making it more suitable for extreme thermal management in complex environments. Our study overcomes the intrinsic structural instability of highly thermally conductive GF in extreme liquid nitrogen environments. Moreover, this research provides inspiration for the development of new materials for future applications and technologies involving extreme liquid nitrogen environments.

Acknowledgements This work is supported by the National Natural Science Foundation of China (Nos. 52272046, 52090030, 52090031, 52122301, 51973191), the Natural Science Foundation of Zhejiang Province (LR23E020003), Shanxi-Zheda Institute of New Materials and Chemical Engineering (2021SZ-FR004, 2022SZ-TD011, 2022SZ-TD012, 2022SZ-TD014), Hundred Talents Program of Zhejiang University (188020*194231701/113, 112300+1944223R3/003, 112300+1944223R3/004), the Fundamental Research Funds for the Central Universities (Nos. 226-2023-00023, 226-2023-00082, 2021FZZX001-17, K20200060), National Key R&D Program of China (NO. 2022YFA1205300, NO. 2022YFA1205301, NO. 2020YFF0204400, NO. 2022YFF0609801), “Pioneer” and “Leading Goose” R&D Program of Zhejiang 2023C01190.

Author Contributions PJZ, YJL, XM, ZX and CG conceived and designed the research. HWL offered all kinds of GFs. PJZ, HS and YYH performed the LNS tests and bubble data statistics of the GFs and the GF@Cu. PJZ, YJL, WDL and JZ prepared the GF@Cu. PJZ, XM and YW performed the simulation experiments.

PJZ, JHL, WWG, WZF and YCC performed the tests of electrical conductivity and thermal conductivity. QYS and YZ conceived the application scenarios. PJZ, XM, HS, ZQW, PL and YXX performed the TEM and SEM characterizations, the tensile tests and another performance characterization. PJZ, XM, and YJL wrote and revised the manuscript.

Declarations

Conflict of interest The authors declare no conflict of interest. They have no known competing financial interests or personal relationships that could have appeared to influence the work reported in this paper. Chao Gao is an editorial board member for Nano-Micro Letters and was not involved in the editorial review or the decision to publish this article.

Open Access This article is licensed under a Creative Commons Attribution 4.0 International License, which permits use, sharing, adaptation, distribution and reproduction in any medium or format, as long as you give appropriate credit to the original author(s) and the source, provide a link to the Creative Commons license, and indicate if changes were made. The images or other third party material in this article are included in the article’s Creative Commons license, unless indicated otherwise in a credit line to the material. If material is not included in the article’s Creative Commons license and your intended use is not permitted by statutory regulation or exceeds the permitted use, you will need to obtain permission directly from the copyright holder. To view a copy of this license, visit <http://creativecommons.org/licenses/by/4.0/>.

Supplementary Information The online version contains supplementary material available at <https://doi.org/10.1007/s40820-023-01277-1>.

References

1. H. Song, J. Liu, B. Liu, J. Wu, H.-M. Cheng et al., Two-dimensional materials for thermal management applications. *Joule* **2**(3), 442–463 (2018). <https://doi.org/10.1016/j.joule.2018.01.006>
2. H.F. Hamann, A. Weger, J.A. Lacey, Z. Hu, P. Bose et al., Hot-spot-limited microprocessors: direct temperature and power distribution measurements. *IEEE J. Solid-State Circuits* **42**(1), 56–65 (2007). <https://doi.org/10.1109/jssc.2006.885064>
3. J.L. Smoyer, P.M. Norris, Brief historical perspective in thermal management and the shift toward management at the nanoscale. *Heat Transf. Eng.* **40**(3–4), 269–282 (2018). <https://doi.org/10.1080/01457632.2018.1426265>
4. A.K. Sikder, N. Sikder, A review of advanced high performance, insensitive and thermally stable energetic materials emerging for military and space applications. *J. Hazard. Mater.* **112**(1–2), 1–15 (2004). <https://doi.org/10.1016/j.jhazmat.2004.04.003>

5. T. Ghidini, Materials for space exploration and settlement. *Nat. Mater.* **17**(10), 846–850 (2018). <https://doi.org/10.1038/s41563-018-0184-4>
6. C. Conficoni, A. Bartolini, A. Tilli, C. Cavazzoni, L. Benini, Integrated energy-aware management of supercomputer hybrid cooling systems. *IEEE Trans. Ind. Inf.* **12**(4), 1299–1311 (2016). <https://doi.org/10.1109/tii.2016.2569399>
7. K. Wirtz, Thermal diffusion in nuclear reactor fuels. *J. Am. Chem. Soc.* **90**(12), 3098–3099 (2002). <https://doi.org/10.1021/ja01014a021>
8. J. Sayers, J. Walker, Nuclear reactor operation in space. *Nature* **211**(5044), 60 (1966). <https://doi.org/10.1038/211060a0>
9. J.A. Aguiar, A.M. Jokisaari, M. Kerr, R. Allen Roach, Bringing nuclear materials discovery and qualification into the 21(st) century. *Nat. Commun.* **11**(1), 2556 (2020). <https://doi.org/10.1038/s41467-020-16406-2>
10. K.F. Man, A.R. Hoffman, Testing of the mars exploration rovers to survive the extreme thermal environments. *J. Microelectron. Electron. Packag.* **4**(4), 145–154 (2007). <https://doi.org/10.4071/1551-4897-4.4.145>
11. Q.F. Guan, H.B. Yang, Z.M. Han, L.C. Zhou, Y.B. Zhu et al., Lightweight, tough, and sustainable cellulose nanofiber-derived bulk structural materials with low thermal expansion coefficient. *Sci. Adv.* **6**(18), eaaz1114 (2020). <https://doi.org/10.1126/sciadv.aaz1114>
12. W.B. Sun, Z.M. Han, X. Yue, H.Y. Zhang, K.P. Yang et al., Nacre-inspired bacterial cellulose/mica nanopaper with excellent mechanical and electrical insulating properties by biosynthesis. *Adv. Mater.* **35**, e2300241 (2023). <https://doi.org/10.1002/adma.202300241>
13. L. Lee, X.C. Cheng, L. Zhang, A high efficiency and low vibration liquid nitrogen cooling system for silicon crystal based x-ray optics. *Rev. Sci. Instrum.* **91**(10), 103105 (2020). <https://doi.org/10.1063/5.0016119>
14. H.X. Xiong, S.H. Yi, H.L. Ding, L. Jin, J.J. Huo, Research on head cooling of high-speed aircraft by liquid nitrogen. *Aeronaut. J.* **125**(1284), 389–409 (2020). <https://doi.org/10.1017/aer.2020.86>
15. K.W. Nam, S.H. Ahn, Crack opening behavior of penetrated crack under fatigue load. *KSME Int. J.* **16**(1), 24–31 (2002). <https://doi.org/10.1007/bf03185152>
16. A.M. Khounsary, R.A. Riddle, A.F. Bernhardt, Microchannel heatsink with liquid-nitrogen cooling. *High Heat Flux Eng.* **1739**, 51–59 (1993). <https://doi.org/10.1117/12.140527>
17. V. Drach, J. Fricke, Transient heat transfer from smooth surfaces into liquid nitrogen. *Cryogenics* **36**(4), 263–269 (1996). [https://doi.org/10.1016/0011-2275\(96\)88785-6](https://doi.org/10.1016/0011-2275(96)88785-6)
18. A.D. Misener, F.T. Hedgcock, Tensile strength of liquid nitrogen. *Nature* **171**(4358), 835–836 (1953). <https://doi.org/10.1038/171835b0>
19. X. Zhong, K. Ruan, J. Gu, Enhanced thermal conductivities of liquid crystal polyesters from controlled structure of molecular chains by introducing different dicarboxylic acid monomers. *Research* **2022**, 9805686 (2022). <https://doi.org/10.34133/2022/9805686>
20. Y. Zhang, C. Lei, K. Wu, Q. Fu, Fully organic bulk polymer with metallic thermal conductivity and tunable thermal pathways. *Adv. Sci.* **8**(14), e2004821 (2021). <https://doi.org/10.1002/advs.202004821>
21. X. Chen, K. Wu, Y. Zhang, D. Liu, R. Li et al., Tropocollagen-inspired hierarchical spiral structure of organic fibers in epoxy bulk for 3D high thermal conductivity. *Adv. Mater.* **34**(40), e2206088 (2022). <https://doi.org/10.1002/adma.202206088>
22. S. Chen, W. Li, X. Li, W. Yang, One-dimensional sic nanostructures: Designed growth, properties, and applications. *Prog. Mater. Sci.* **104**, 138–214 (2019). <https://doi.org/10.1016/j.pmatsci.2019.04.004>
23. V. Guerra, C. Wan, T. McNally, Thermal conductivity of 2d nano-structured boron nitride (bn) and its composites with polymers. *Prog. Mater. Sci.* **100**, 170–186 (2019). <https://doi.org/10.1016/j.pmatsci.2018.10.002>
24. Y. Yang, X. Huang, Z. Cao, G. Chen, Thermally conductive separator with hierarchical nano/microstructures for improving thermal management of batteries. *Nano Energy* **22**, 301–309 (2016). <https://doi.org/10.1016/j.nanoen.2016.01.026>
25. M.S.B. Hoque, Y.R. Koh, J.L. Braun, A. Mamun, Z. Liu et al., High in-plane thermal conductivity of aluminum nitride thin films. *ACS Nano* **15**(6), 9588–9599 (2021). <https://doi.org/10.1021/acsnano.0c09915>
26. J. Wang, D. Liu, Q. Li, C. Chen, Z. Chen et al., Lightweight, superelastic yet thermoconductive boron nitride nanocomposite aerogel for thermal energy regulation. *ACS Nano* **13**(7), 7860–7870 (2019). <https://doi.org/10.1021/acsnano.9b02182>
27. J. Wang, Y. Wu, Y. Xue, D. Liu, X. Wang et al., Super-compatible functional boron nitride nanosheets/polymer films with excellent mechanical properties and ultra-high thermal conductivity for thermal management. *J. Mater. Chem. C* **6**(6), 1363–1369 (2018). <https://doi.org/10.1039/c7tc04860b>
28. J. Wang, T. Yang, Z. Wang, X. Sun, M. An et al., A thermochromic, viscoelastic nacre-like nanocomposite for the smart thermal management of planar electronics. *Nano-Micro Lett.* **15**(1), 170 (2023). <https://doi.org/10.1007/s40820-023-01149-8>
29. J. Wang, Q. Li, D. Liu, C. Chen, Z. Chen et al., High temperature thermally conductive nanocomposite textile by “green” electrospinning. *Nanoscale* **10**(35), 16868–16872 (2018). <https://doi.org/10.1039/c8nr05167d>
30. A.L. Woodcraft, Recommended values for the thermal conductivity of aluminum of different purities in the cryogenic to room temperature range, and a comparison with copper. *Cryogenics* **45**(9), 626–636 (2005). <https://doi.org/10.1016/j.cryogenics.2005.06.008>
31. Q. Shen, M. Jiang, R. Wang, K. Song, M.H. Vong et al., Liquid metal-based soft, hermetic, and wireless-communicable seals for stretchable systems. *Science* **379**(6631), 488–493 (2023). <https://doi.org/10.1126/science.ade7341>
32. M.H. Malakooti, N. Kazem, J. Yan, C. Pan, E.J. Markvicka et al., Liquid metal supercooling for low-temperature thermoelectric wearables. *Adv. Funct. Mater.* **29**(45), 1906098 (2019). <https://doi.org/10.1002/adfm.201906098>



33. G. Xin, T. Yao, H. Sun, S.M. Scott, D. Shao et al., Highly thermally conductive and mechanically strong graphene fibers. *Science* **349**(6252), 1083–1087 (2015). <https://doi.org/10.1126/science.aaa6502>
34. J. Zhong, W. Sun, Q. Wei, X. Qian, H.M. Cheng et al., Efficient and scalable synthesis of highly aligned and compact two-dimensional nanosheet films with record performances. *Nat. Commun.* **9**(1), 3484 (2018). <https://doi.org/10.1038/s41467-018-05723-2>
35. X. Ming, A. Wei, Y. Liu, L. Peng, P. Li et al., 2D-topology-seeded graphitization for highly thermally conductive carbon fibers. *Adv. Mater.* **34**(28), e2201867 (2022). <https://doi.org/10.1002/adma.202201867>
36. F. Wang, W. Fang, X. Ming, Y. Liu, Z. Xu et al., A review on graphene oxide: 2d colloidal molecule, fluid physics, and macroscopic materials. *Appl. Phys. Rev.* **10**(1), 0128899 (2023). <https://doi.org/10.1063/5.0128899>
37. W. Dai, T. Ma, Q. Yan, J. Gao, X. Tan et al., Metal-level thermally conductive yet soft graphene thermal interface materials. *ACS Nano* **13**(10), 11561–11571 (2019). <https://doi.org/10.1021/acsnano.9b05163>
38. L. Peng, Z. Xu, Z. Liu, Y. Guo, P. Li et al., Ultrahigh thermal conductive yet superflexible graphene films. *Adv. Mater.* **29**(27), 1700589 (2017). <https://doi.org/10.1002/adma.201700589>
39. H. Huang, X. Ming, Y. Wang, F. Guo, Y. Liu et al., Polyacrylonitrile-derived thermally conductive graphite film via graphene template effect. *Carbon* **180**, 197–203 (2021). <https://doi.org/10.1016/j.carbon.2021.04.090>
40. Z. Han, J. Wang, S. Liu, Q. Zhang, Y. Liu et al., Electrospinning of neat graphene nanofibers. *Adv. Fiber. Mater.* **4**(2), 268–279 (2021). <https://doi.org/10.1007/s42765-021-00105-8>
41. S. Luo, L. Peng, Y. Xie, X. Cao, X. Wang et al., Flexible large-area graphene films of 50–600 nm thickness with high carrier mobility. *Nano-Micro Lett.* **15**(1), 61 (2023). <https://doi.org/10.1007/s40820-023-01032-6>
42. M. Cao, S. Liu, Q. Zhu, Y. Wang, J. Ma et al., Monodomain liquid crystals of two-dimensional sheets by boundary-free sheargraphy. *Nano-Micro Lett.* **14**(1), 192 (2022). <https://doi.org/10.1007/s40820-022-00925-2>
43. P. Liu, X. Li, P. Min, X. Chang, C. Shu et al., 3d lamellar-structured graphene aerogels for thermal interface composites with high through-plane thermal conductivity and fracture toughness. *Nano-Micro Lett.* **13**(1), 22 (2020). <https://doi.org/10.1007/s40820-020-00548-5>
44. W. Dai, X.J. Ren, Q. Yan, S. Wang, M. Yang et al., Ultralow interfacial thermal resistance of graphene thermal interface materials with surface metal liquefaction. *Nano-Micro Lett.* **15**(1), 9 (2022). <https://doi.org/10.1007/s40820-022-00979-2>
45. C.P. Feng, F. Wei, K.Y. Sun, Y. Wang, H.B. Lan et al., Emerging flexible thermally conductive films: Mechanism, fabrication, application. *Nano-Micro Lett.* **14**(1), 127 (2022). <https://doi.org/10.1007/s40820-022-00868-8>
46. I. Gouzman, E. Grossman, R. Verker, N. Atar, A. Bolker et al., Advances in polyimide-based materials for space applications. *Adv. Mater.* **31**(18), e1807738 (2019). <https://doi.org/10.1002/adma.201807738>
47. A. Norman, S. Das, T. Rohr, T. Ghidini, Advanced manufacturing for space applications. *CEAS Space J.* **15**(1), 1–6 (2022). <https://doi.org/10.1007/s12567-022-00477-6>
48. H.A. Atwater, A.R. Davoyan, O. Ilic, D. Jariwala, M.C. Sherrott et al., Materials challenges for the starshot lightsail. *Nat. Mater.* **17**(10), 861–867 (2018). <https://doi.org/10.1038/s41563-018-0075-8>
49. S. Wan, X. Li, Y. Chen, N. Liu, Y. Du et al., High-strength scalable mxene films through bridging-induced densification. *Science* **374**(6563), 96–99 (2021). <https://doi.org/10.1126/science.abg2026>
50. S. Wan, Y. Chen, S. Fang, S. Wang, Z. Xu et al., High-strength scalable graphene sheets by freezing stretch-induced alignment. *Nat. Mater.* **20**(5), 624–631 (2021). <https://doi.org/10.1038/s41563-020-00892-2>
51. K. Shen, P. Li, J. Lin, Z. Wang, G. Cai et al., Intercalated oligomer doubles plasticity for strong and conductive graphene papers and composites. *Carbon* **208**, 160–169 (2023). <https://doi.org/10.1016/j.carbon.2023.03.036>
52. P. Li, M. Yang, Y. Liu, H. Qin, J. Liu et al., Continuous crystalline graphene papers with gigapascal strength by intercalation modulated plasticization. *Nat. Commun.* **11**, 2645 (2020). <https://doi.org/10.1038/s41467-020-16494-0>
53. P.A. Misra, I. Manousakis, E. Choukse, M. Jalili, I. Goiri et al., Overclocking in immersion-cooled datacenters. *IEEE Micro* **42**(4), 10–17 (2022). <https://doi.org/10.1109/mm.2022.3163107>
54. K. Pang, X. Song, Z. Xu, X. Liu, Y. Liu et al., Hydroplastic foaming of graphene aerogels and artificially intelligent tactile sensors. *Sci. Adv.* **6**(46), eabd4045 (2020). <https://doi.org/10.1126/sciadv.abd4045>
55. J. Wang, A.V. Nguyen, S. Farrokhpay, A critical review of the growth, drainage and collapse of foams. *Adv. Colloid Interface Sci.* **228**, 55–70 (2016). <https://doi.org/10.1016/j.cis.2015.11.009>
56. L. Li, J. Xu, G. Li, X. Jia, Y. Li et al., Preparation of graphene nanosheets by shear-assisted supercritical CO₂ exfoliation. *Chem. Eng. J.* **284**, 78–84 (2016). <https://doi.org/10.1016/j.cej.2015.08.077>
57. Z. Sun, Q. Fan, M. Zhang, S. Liu, H. Tao et al., Supercritical fluid-facilitated exfoliation and processing of 2d materials. *Adv. Sci.* **6**(18), 1901084 (2019). <https://doi.org/10.1002/adv.201901084>
58. D.-J. Liaw, K.-L. Wang, Y.-C. Huang, K.-R. Lee, J.-Y. Lai et al., Advanced polyimide materials: syntheses, physical properties and applications. *Prog. Polym. Sci.* **37**(7), 907–974 (2012). <https://doi.org/10.1016/j.progpolymsci.2012.02.005>
59. K. Yang, Z. Zhang, H. Zhao, B. Yang, B. Zhong et al., Orientation independent heat transport characteristics of diamond/copper interface with ion beam bombardment. *Acta Mater.* **220**, 117283 (2021). <https://doi.org/10.1016/j.actamat.2021.117283>
60. Z. Wei, W. Ju, K. Bi, J. Yang, Y. Chen, Significant enhancement of thermal boundary conductance in graphite/al interface by ion intercalation. *Int. J. Heat Mass Transf.* **157**, 119946

- (2020). <https://doi.org/10.1016/j.ijheatmasstransfer.2020.119946>
61. K.M. Yang, Y.C. Ma, Z.Y. Zhang, J. Zhu, Z.B. Sun et al., Anisotropic thermal conductivity and associated heat transport mechanism in roll-to-roll graphene reinforced copper matrix composites. *Acta Mater.* **197**, 342–354 (2020). <https://doi.org/10.1016/j.actamat.2020.07.021>
 62. M. Blank, L. Weber, Influence of interfacial structural disorder and/or chemical interdiffusion on thermal boundary conductance for ti/si and au/si couples. *J. Appl. Phys.* **126**(15), 155302 (2019). <https://doi.org/10.1063/1.5114671>
 63. C.-J. Twu, J.-R. Ho, Molecular-dynamics study of energy flow and the kapitza conductance across an interface with imperfection formed by two dielectric thin films. *Phys. Rev. B* **67**(20), 205422 (2003). <https://doi.org/10.1103/PhysRevB.67.205422>
 64. J. Wang, Z. Wang, K. Yang, N. Chen, J. Ni et al., Enhanced heat transport capability across boron nitride/copper interface through inelastic phonon scattering. *Adv. Funct. Mater.* **32**(40), 2206545 (2022). <https://doi.org/10.1002/adfm.202206545>
 65. X.D. Zhang, G. Yang, B.Y. Cao, Bonding-enhanced interfacial thermal transport: Mechanisms, materials, and applications. *Adv. Mater. Interfaces* **9**(27), 2200078 (2022). <https://doi.org/10.1002/admi.202200078>
 66. Y. Liu, J. Guo, E. Zhu, L. Liao, S.J. Lee et al., Approaching the schottky-mott limit in van der waals metal-semiconductor junctions. *Nature* **557**(7707), 696–700 (2018). <https://doi.org/10.1038/s41586-018-0129-8>
 67. M. Cao, D.B. Xiong, L. Yang, S. Li, Y. Xie et al., Ultrahigh electrical conductivity of graphene embedded in metals. *Adv. Funct. Mater.* **29**(17), 1806792 (2019). <https://doi.org/10.1002/adfm.201806792>
 68. H. Peng, X. Ming, K. Pang, Y. Chen, J. Zhou et al., Highly electrically conductive graphene papers via catalytic graphitization. *Nano Res.* **15**(6), 4902–4908 (2022). <https://doi.org/10.1007/s12274-022-4130-z>
 69. S. Zhang, X. Liu, C. Jia, Z. Sun, H. Jiang et al., Integration of multiple heterointerfaces in a hierarchical 0D@2D@1D structure for lightweight, flexible, and hydrophobic multifunctional electromagnetic protective fabrics. *Nano-Micro Lett.* **15**, 204 (2023). <https://doi.org/10.1007/s40820-023-01179-2>
 70. Z. Nan, W. Wei, Z. Lin, J. Chang, Y. Hao, Flexible nanocomposite conductors for electromagnetic interference shielding. *Nano-Micro Lett.* **15**, 172 (2023). <https://doi.org/10.1007/s40820-023-01122-5>

